ADVANCED FUNCTIONAL MATERIALS
www.afm-journal.de

Synthesis of Leaf-Vein-Like g-C_3N_4 with Tunable Band Structures and Charge Transfer Properties for Selective Photocatalytic H_2O_2 Evolution

Chengyang Feng, Lin Tang, Yaocheng Deng, Jiajia Wang, Jun Luo, Yani Liu, Xilian Ouyang, Haoran Yang, Jiangfang Yu, and Jingjing Wang*

Photocatalytic H_2O_2 evolution through two-electron oxygen reduction has attracted wide attention as an environmentally friendly strategy compared with the traditional anthraquinone or electrocatalytic method. Herein, a biomimetic leaf-vein-like g-C_3N_4 as an efficient photocatalyst for H_2O_2 evolution is reported, which owns tenable band structure, optimized charge transfer, and selective two-electron O_2 reduction. The mechanism for the regulation of band structure and charge transfer is well studied by combining experiments and theoretical calculations. The H_2O_2 yield of CN4 (287 µmol h^{-1}) is about 3.3 times higher than that of pristine CN (87 µmol h^{-1}), and the apparent quantum yield for H_2O_2 evolution over CN4 reaches 27.8% at 420 nm, which is much higher than that for many other current photocatalysts. This work not only provides a novel strategy for the design of photocatalyst with excellent H_2O_2 evolution efficiency, but also promotes deep understanding for the role of defect and doping sites on photocatalytic activity.

1. Introduction

Hydrogen peroxide (H_2O_2) is an important clean chemical resource that emits only water as by-product and is widely used in organic synthesis, wastewater treatment, pulp bleaching, disinfection, and other fields.[1] Recently, H_2O_2 has also received much attention as a promising substitute for hydrogen in single-compartment cells for electricity generation.[2] The huge demand for H_2O_2 has raised people's attention to the preparation technology of H_2O_2, meanwhile, the most widely used anthraquinone method is faced with the disadvantages of high energy consumption and substantial toxic by-products, so the development of clean preparation technology for H_2O_2 is urgent.[3] Photocatalytic H_2O_2 preparation with semiconductor catalysts has attracted much attention due to its clean and low-energy light driven two-electron O_2 reduction process ($O_2 + 2H^+ + 2e^- \rightarrow H_2O_2$).[4] This two-electron oxygen reduction process is proved to consist of a two-step single-electron reduction with superoxide radical ($\cdot O_2^-$) as the intermediate product ($O_2 + e^- \rightarrow \cdot O_2^-$ and $\cdot O_2^- + 2H^+ + e^- \rightarrow H_2O_2$).[5] However, its H_2O_2 formation efficiency is usually very low, which may be limited by the second step from $\cdot O_2^-$ to H_2O_2. The low conversion efficiency of $\cdot O_2^-$ to H_2O_2 will result in a large number of photoexcited electrons only participating in the single-electron oxygen reduction process ($O_2 + e^- \rightarrow \cdot O_2^-$), greatly reducing the utilization of light energy. Hence, enhancing the selectivity of the two-electron photocatalytic O_2 reduction process is the key to improve the efficiency of photocatalytic H_2O_2 production.

Graphitic carbon nitride (g-C_3N_4), as a stable and low-cost metal-free polymeric semiconductor, has recently attracted wide attention owing to its excellent photocatalytic performance for water splitting,[6] CO_2 reduction,[7] nitrogen fixation,[8] and organic pollutant degradation.[9] In addition, recent studies have found that g-C_3N_4 also showed prominent potential for photocatalytic H_2O_2 production.[10] The reaction is usually carried out with light irradiation in O_2-saturated water in the presence of hole acceptor such as alcohols, where the photoexcited holes (h^+) oxidize alcohol into aldehyde and release protons while the photoexcited electrons (e^-) promote the oxygen reduction process with the help of released protons. However, pristine g-C_3N_4 has a limited photocatalytic activity due to its insufficient visible-light absorption range, serious charge recombination, and mediocre surface charge transfer efficiency. Fortunately, the preparation of g-C_3N_4 is easy to regulate, which facilitates the optimization of its photocatalytic properties. Up to now, a variety of strategies have been developed to overcome these shortcomings, such as morphology control,[11] heteroatoms doping,[12] or coupling with other semiconductors.[13] Recently, the introduction of defects into the heptazine framework of

C. Feng, Prof. L. Tang, Dr. J. Wang, J. Luo, Y. Liu, X. Ouyang, H. Yang, J. Yu, J. Wang
College of Environmental Science and Engineering
Key Laboratory of Environmental Biology and Pollution Control
Hunan University
Changsha 410082, China
E-mail: tanglin@hnu.edu.cn
Prof. Y. Deng
College of Resources and Environment
Hunan Agricultural University
Changsha 410028, China
The ORCID identification number(s) for the author(s) of this article can be found under https://doi.org/10.1002/adfm.202001922.

DOI: 10.1002/adfm.202001922

g-C_3N_4 has attracted researchers' interest, it is found that the light absorption and charge separation capacity of g-C_3N_4 can be controlled by changing the content of defects.[14] Defect modified g-C_3N_4 shows excellent activities in H_2 evolution and CO_2 reduction, so we believe it can still perform well in H_2O_2 production. Meanwhile, although the promotion effect of defects on light absorption and charge separation has been proved in previous literatures, the theoretical study on the mechanism of its promotion is relatively lacking. Hence, we plan to construct defect modified g-C_3N_4 for H_2O_2 production, and further study its mechanism with density-functional-theory (DFT) calculation based on experimental phenomena.

Herein, we describe a novel one step KBH_4-assisted thermal polymerization for the modification of g-C_3N_4. Characterization indicates that this method can achieve boron doping while introducing defects. By controlling the dosage of KBH_4, the light absorption, charge separation, and surface charge transfer capacity of g-C_3N_4 can be regulated easily and effectively. DFT calculation proved that there is a synergistic effect between defect and doped boron atom, which can greatly improve the photocatalytic performance of g-C_3N_4. In addition, an interesting morphological change can be observed by SEM, TEM, and AFM. With the presence of KBH_4, the surface of g-C_3N_4 changes from smooth to a folded structure similar to the leaf vein, which can greatly increase the specific surface area and expose more reactive sites. The prepared photocatalyst exhibited a remarkably high H_2O_2 evolution rate (574×10^{-6} M h^{-1} g^{-1}) with apparent quantum efficiency up to 27.8% at 420 nm, which is much higher than other current literature values. The excellent H_2O_2 evolution capacity is not only due to the wider light response and higher charge transfer capacity of g-C_3N_4 after modified, but also attributed to the higher selectivity of two-electron oxygen reduction process, which effectively reduces the accumulation of intermediates ($\cdot O_2^-$) and greatly improves the conversion rate of light to H_2O_2. We believe that this work puts forward new ideas for understanding the mechanism by which defects and doping sites improve the photocatalytic performance of g-C_3N_4, and provides a novel and promising solution to design and develop photocatalyst for H_2O_2 evolution and other photocatalytic fields.

2. Results and Discussion

The chemical structure of prepared CN and CN*x* samples was first characterized by XRD patterns. As shown in **Figure 1**a, the CN and CN*x* samples showed similar XRD patterns with two distinct diffraction peaks at 13.0° and 27.4°, which can be assigned to the in-plane packed heptazine units (1 0 0) and π–π interlayer stacking (0 0 2) of g-C_3N_4. A gradual weakening can be observed on both the two peaks with the increase of KBH_4 usage, indicating the loss of ordered structures within the interlayer stacking and heptazine framework to some extent. These structure changes may result from the reaction between molecular precursors and KBH_4 during the thermal-polymerization process. More detailed chemical structure changes of CN and CN*x* samples were identified by FTIR spectroscopy. As shown in Figure 1b, the peak at 808 cm^{-1} refers to the out-of-plane bending mode of heptazine rings of g-C_3N_4, and the peaks located in the region of 1200–1650 cm^{-1} can be assigned to the stretching vibration modes of C—N and C=N heterocycles in g-C_3N_4 framework. On the one hand, the retention of these peaks in CN*x* represents the preservation of the framework structures. On the other hand, the novel and gradually enhanced peak at 2177 cm^{-1} in CN*x* indicates the introduction of cyano groups (C≡N) with the presence of KBH_4. The emergence of –C≡N groups may be attributed to the reduction of melamine-derived intermediates in the strong reducing atmosphere caused by KBH_4 at high temperature.

XPS analysis was performed to further investigate the effect of KBH_4 treatment on the chemical state and composition of CN*x* samples. The very similar XPS survey spectra (Figure S1, Supporting Information) indicate basically the same elemental composition of CN and CN*x*. However, the narrow scan B 1s spectra (Figure 1c) show that B was introduced into the CN*x* samples. The B 1s peak increases and shifts to lower binding energy gradually with the increase of KBH_4. The B 1s spectra exhibit main binding energy at about 190.0 eV, which is located within the binding energy range of B—C bond,[15] suggesting the formation of B—C bond in CN*x* samples. The atomic ratios of C, N, and B of CN and CN*x* samples can be determined by XPS analysis and displayed in Figure S2 (Supporting Information). Obviously, with the increase of KBH_4 dosage, the atomic ratio of N decreased from 57.08% to 47.62%, and the atomic ratio of B increased from 0% to 12.44%. By contrast, the change of C atomic ratio is small, falling by only 2.98%. Given that the reduction in N atomic is very close to the increase in B atomic, it is reasonable to assume that B is successfully doped in g-C_3N_4 and replaced N in the heptazine structure. In addition, the element ratio of prepared samples was also determined by OEA and ICP-OES. As shown in Figure S3 (Supporting Information), the N/C atomic ratio decreased from 1.433 to 1.285 with the increase of KBH_4 dosage, indicating a gradual decrease in N content. Meanwhile, the B atom content went from 0% to 9.879%, revealing the substitution of B for N. Figure 1d,e shows the high-resolution C 1s and N 1s spectra for CN and CN*x* samples. The C 1s spectra for CN can be divided into three peaks at 288.1, 286.4, and 284.6 eV, corresponding to N—C=N bond, C—NH_x group and adsorbed hydrocarbons, respectively.[16] Obviously, the C—NH_x peak increased gradually with the KBH_4 dosage enhanced, which is consistent with the conclusion above that C≡N was introduced in the framework since C≡N exhibits similar C 1s binding energy to C—NH_x.[18a] As for N 1s spectra, there are three component peaks at 398.5, 400.3, and 401.1 eV for pristine CN corresponding to bi-coordinated N (C—N=C), tri-coordinated N (N—3C), and NH*x* groups in the heptazine framework, respectively.[17] The relative intensity of N–3C peak enhanced with increasing KBH_4 usage during the thermal polymerization, indicating the change of the relative content of nitrogen atoms in N—3C and C—N=C. The corresponding atomic ratios of nitrogen in N—3C and C—N=C were obtained by fitting the N 1s spectra and illustrated in Figure S4 (Supporting Information). Apparently, the bi-coordinated N decreased while the tri-coordinated N increased with the increase of KBH_4 dosage, and combined with the conjecture that B replaced N, the introduced B is more likely to replace N in C—N=C group. In addition, with the increase of B doping, the B 1s peak shifts to lower binding energy while both the

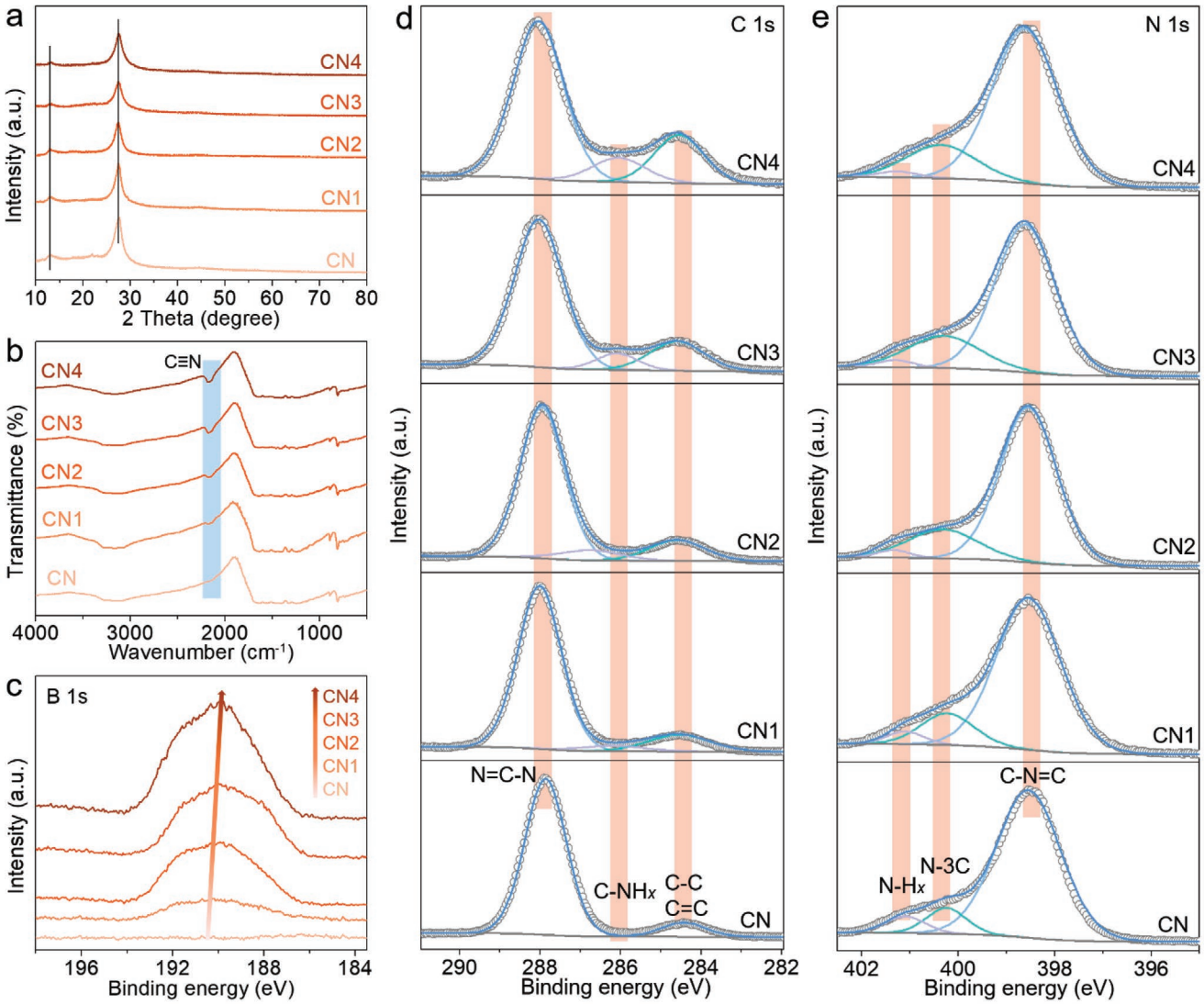

Figure 1. a) XRD patterns and b) FTIR transmission spectra of CN and CN*x*. The c) B 1s, d) C 1s, and e) N 1s high resolution XPS spectra of CN and CN*x*.

C 1s and N 1s peaks exhibit a shift to higher binding energy, respectively, which is due to the fact that the introduced B has fewer valence electron compared to the replaced N, causing a redistribution of electron density in the heptazine framework. The electron in heptazine unit tended to transfer to B, resulting in the increased electron density on B and decreased electron density on C and N. As the higher electron density corresponds to lower XPS binding energy, the shift for XPS peaks of C, N, and B matches the change in electron density perfectly. And the redistribution of electrons caused by B will facilitate the separation of photoexcited charge carriers, which is discussed below.

The morphologies and microstructures of prepared samples were observed by SEM. Figures S5–S9 (Supporting Information) display the SEM images of CN and CN*x* samples. The pristine CN sample shows bulk-like structure with smooth surface, however, with the assistance of KBH_4, the prepared CN*x* samples exhibit sheet-like structure with wrinkle (selected with rectangles) and pore (selected with circles) on the surface, just like the leaf-vein of savoy (**Scheme 1**). The morphologies of samples were also confirmed by TEM images. As shown in Figure S10a–e (Supporting Information), the pristine CN has a smooth surface and no pore structure, but the modified CN*x* samples all possessed sheet-like structure with wrinkles, which is deepened with the increase of KBH_4 dosage. The TEM image in Figure S10e (Supporting Information) shows the abundant pore structure of CN4 samples. These pores extending from the inside of g-C_3N_4 are derived from the channels left by the escaped H_2 generated internally during the polymerization process. AFM 3D images (Figure S11, Supporting Information) also confirmed a significant increase in the roughness of the modified samples. Considering that the leaf-vein-like surface and pore structure could increase the specific surface area, N_2 adsorption–desorption measurements were performed. As shown in Figure S13a (Supporting Information), the BET specific surface area of pristine CN is determined to be 43.6 $m^2\ g^{-1}$, which is relatively small due to its bulk-like structure. However, the BET specific surface area of CN*x* are much higher than that of pristine CN and increased progressively on the going

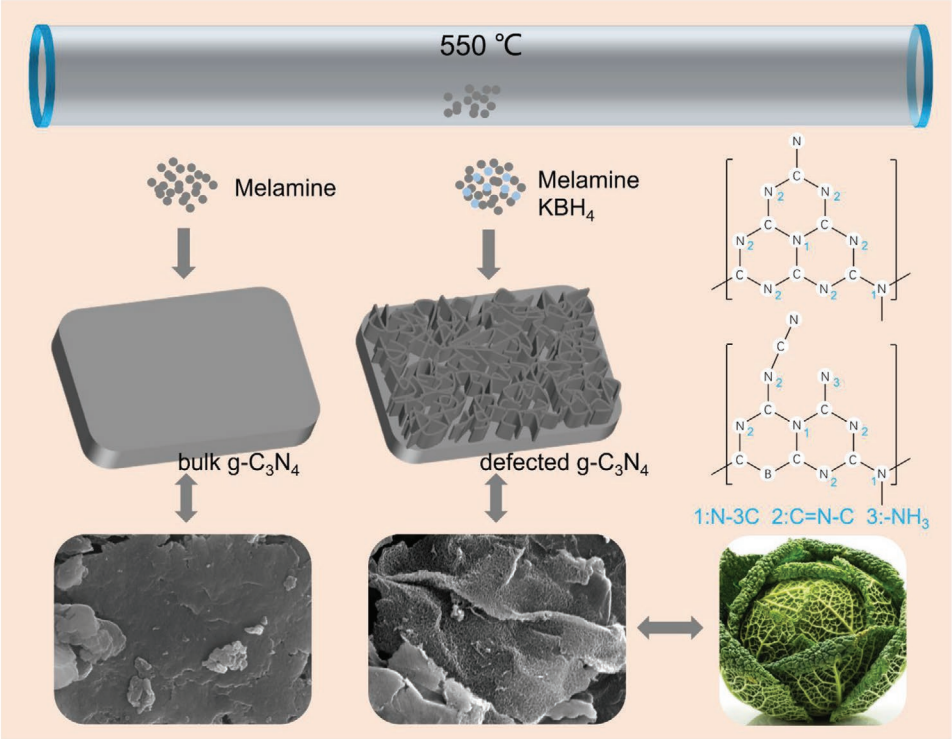

Scheme 1. Schematic illustration for the preparation of leaf-vein-like g-C_3N_4.

from CN1 to CN4, indicating that the increase of KBH_4 can significantly change the morphology of CN*x*. The BJH pore size distributions of prepared samples were also obtained and displayed in Figure S13b (Supporting Information). The pristine CN sample has almost no pore structure due to its bulk-like morphology, while the CN*x* samples own abundant pores distributed in the range from 15 to 60 nm, which is produced by the escape of H_2 during the reaction. In addition, the pore diameter and content both increased with the increase of KBH_4 dosage. As expected, the large specific surface area and abundant pore structure can expose more reactive sites, provide larger light receiving areas and increase light absorption capacity, thus further enhancing the photocatalytic performance. Hence, the preparation of CN*x* and formation process of leaf-vein-like structure can be proposed and illustrated in Scheme 1 and Figure S12 (Supporting Information). Without KBH_4, the molecular precursors polymerize and stack layer upon layer to form bulk-like g-C_3N_4 with smooth surface during the thermal-polymerization process under N_2 atmosphere. And when KBH_4 was added, it breaks down at high temperature and releases H_2. The released H_2 gas will leave pores on the surface of g-C_3N_4 and create a reducing atmosphere at high temperature, resulting in the defects on g-C_3N_4 and the formation of leaf-vein-like structure. As shown on the right of Scheme 1, the heptazine units were reduced to form C≡N groups and introduce framework defect sites, on the other hand, B replace the N atom in C=N−C groups to form doping sites, which can both decrease the atomic ratios of N in C=N−C. The chemical structure with defect and doping sites obtained here will be used as the model basis for the theoretical simulations.

To examine the effect of KBH_4 addition on the optical adsorption and band structure of CN*x*, the UV–vis diffuse reflectance spectroscopy (DRS) was measured. As shown in **Figure 2**a, a progressive redshift in the absorption edge can be observed with increasing KBH_4 usage. Compared to pristine CN, the CN*x* samples not only exhibit enhanced intrinsic absorption bands originating from the $\pi \rightarrow \pi^*$ electron transition of the sp^2 hybridization conjugated aromatic rings, but also exhibit new absorption bands ascribed to the $n \rightarrow \pi^*$ electron transition of the lone pair electrons of defect sites (C≡N).[18] Based on the DRS data, the corresponding bandgaps of prepared samples were determined by the transformed Kubelka–Munk function as shown in Figure 2b. Bandgaps of CN and CN*x* progressively narrowed from 2.65 to 2.33 eV, revealing the gradual enhancement of optical response ability. To understand the bandgap narrowing in the CN*x* samples, the XPS valence band (VB) spectra were measured. As shown in Figure 2c, the determined VB potential for both CN and CN*x* samples was located at about 1.93 eV, which was not influenced by the addition of KBH_4. After eliminating the measurement error by the following formula with the work function (Φ) of XPS analyzer and vacuum level to be 3.88 and 4.44 eV (vs NHE), the VB of CN and CN*x* were calculated to be 1.37 eV (vs NHE).

$$\mathrm{VB(vs\ NHE)} = \Phi + 1.93\ \mathrm{eV} - 4.44 \quad (1)$$

Combining with the obtained bandgaps, the conduction band (CB) potentials of CN and CN1–4 can be determined to be −1.28, −1.25, −1.14, −1.10, and −0.96 eV (vs NHE), with the band structure comparison shown in Figure 2d.

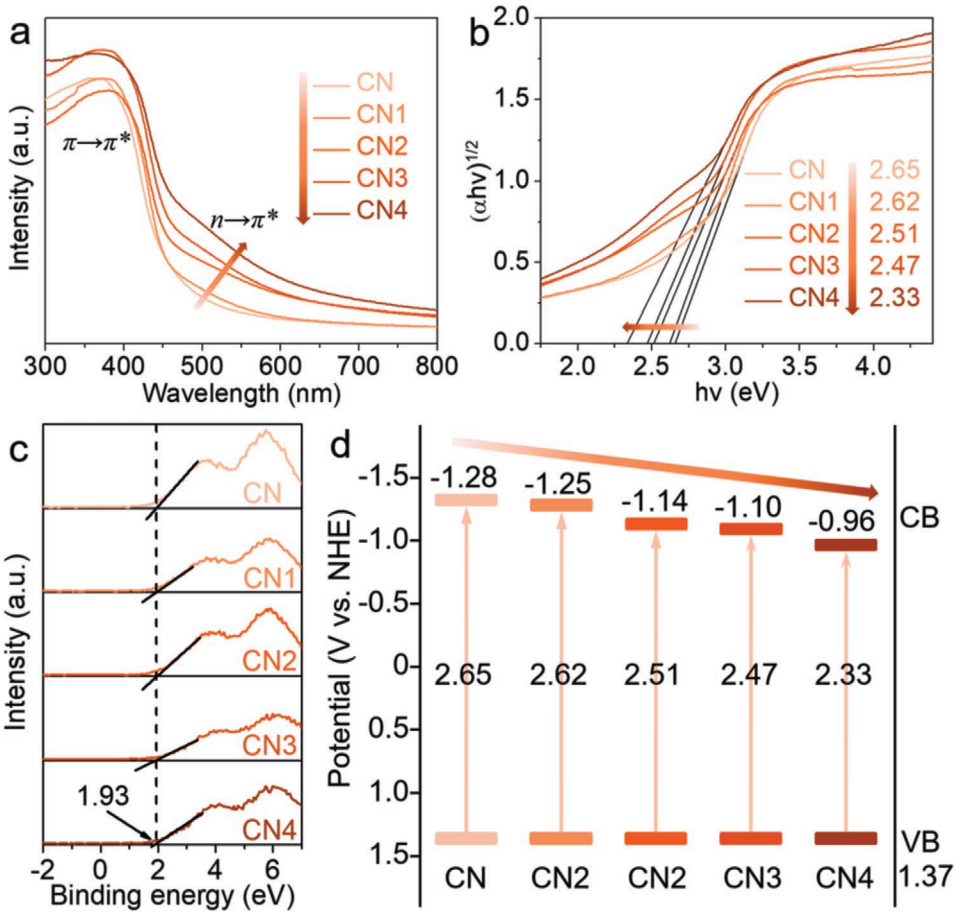

Figure 2. a) UV–vis DRS and b) corresponding plots of transformed Kubelka–Munk function versus photon energy of CN and CN*x*. c) XPS valence band spectra of CN and CN*x*. d) The estimated band structure of CN and CN*x*.

In order to understand the contribution of defect modification and B doping to the bandgap narrowing, DFT calculation for the density of states (DOS) was first performed. As shown in **Figure 3**a_1–c_1, both the defect and B doping cause the downward shift of CB and result in the narrower bandgap compared to the pristine g-C_3N_4. The obtained bandgaps of pristine g-C_3N_4, defected g-C_3N_4, and B-doped defected g-C_3N_4 are 1.56, 1.25, and 0.71, respectively. Figure 3a_2–c_2 illustrates the corresponding DOS for orbitals. Figure 3a_2 shows that the VB of pristine g-C_3N_4 is mainly composed of N p-orbitals, while the CB is contributed by p-orbitals of C and N. After the introduction of defects, the bandgap is narrower than that of pristine g-C_3N_4 (Figure 3b_2). And when a B atom is doped in the framework of g-C_3N_4 and replaces a N atom, further narrowing can be observed, and the contribution of C p-orbitals to the CB composition increases, which may be due to the decrease of N content. To further understand the relationships among defect, doped B, and the changed band structure, a two-layer g-C_3N_4 model with isolated defect and B doping sites were established to calculate the 3D visualization of VBM (valence band maximum) and CBM (conduction band minimum). As shown in **Figure 4**a, the VBM and CBM were determined by both two layers of pristine g-C_3N_4, exhibiting high homogeneity. When the defect was introduced, the VBM was determined by the non-defected layer while the CBM was located at defected layer, revealing that the presence of defects can rearrange the band structure and facilitate charge separation. And after the introduction of B, as shown in Figure 4c, the distribution of VB around B doped sites increases obviously and even affects the defect sites in the upper layer, which may be related to the enhanced density of excitable electrons around B caused by its electron receptor effect.

In addition to effect the band structure, the introduction of defect and B doping sites also influences the separation efficiency of photoexcited charge carriers. The room temperature PL spectroscopy measurement of CN and CN*x* samples was performed with an excitation wavelength of 375 nm. As shown in **Figure 5**a, the CN sample exhibits intense PL signal due to its intrinsic serious charge recombination, while the PL intensity decreases progressively with the increasing of KBH_4 dosage, confirming that the introduction of defect and B doping sites is highly beneficial for the separation of photoexcited charges in CN*x*. Figure S14 (Supporting Information) shows the time-resolved fluorescence spectra of CN and CN*x* samples. The calculated average emission lifetime of CN samples is 6.4181 ns, and the calculated lifetime of CN*x* increased significantly and gradually from 7.4113 to 8.2610 ns with the increase of KBH_4 dosage, indicating that the introduction of

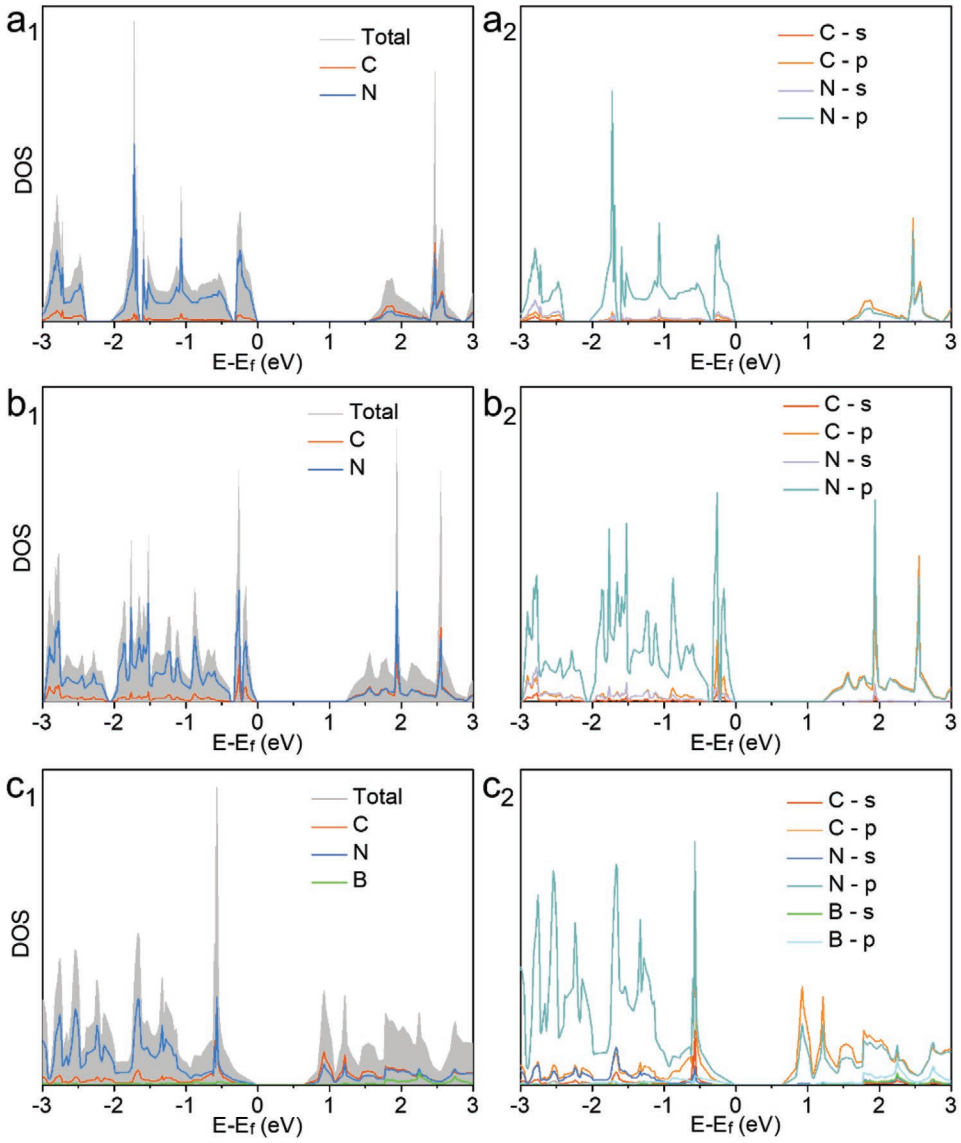

Figure 3. DOS of a) pristine g-C_3N_4, b) defected g-C_3N_4, and c) B-doped defected g-C_3N_4: 1) Total DOS and DOS for elements, 2) DOS for orbitals.

defect and B doping sites can promote the charge transfer and separation, and thus enhance the charge lifetime. Figure 5b shows the electrochemical impedance spectroscopy (EIS) of CN and CN*x* samples under visible light irradiation. The decreased EIS slop of CNx reflects the lower electric resistance compared to the CN sample, which is beneficial for the charge transfer. Transient photocurrent responses of CN and CN*x* reveal that the CN*x* samples can excite more electron–hole pairs under visible light, and the current density increased gradually from CN1 to CN4, which is consistent with the trend of the charge separation enhancement confirmed above. The photocurrent densities of CN and CN4 with different electrode film thicknesses were measured to evaluate the charge transfer capacity, where the electrode film thickness was regulated by controlling the concentration of catalyst suspension. As shown in Figure 5d, the current densities are concentration-dependent and reach maximum at 0.139 and 0.335 μA cm^{-1} for CN (6 g L^{-1}) and CN4 (10 g L^{-1}), respectively. The optimum concentration is determined by the light absorption and charge transfer capacity. In the rising period, light absorption limits the photocurrent, while in the decline stage, electron transport to the FTO is the limiting factor. So, the data indicate that the electron diffusion length is enhanced in CN4 compared to the pristine CN samples. All the above results confirm that the CN*x* exhibit optimized charge separation and transfer efficiency compared to the pristine CN, which can greatly improve the photocatalytic performance. In addition, compared with defective or B-doped g-C_3N_4, the co-modification shows a stronger charge separation promotion (Figure S15a, Supporting Information), suggesting a synergistic effect between defect and B-doping sites.

Since the barrier to the charge separation of g-C_3N_4 is primarily the interlaminar space, in order to understand the relationship between the enhanced charge separation efficiency and the introduction of defect and B, the 3D charge density and

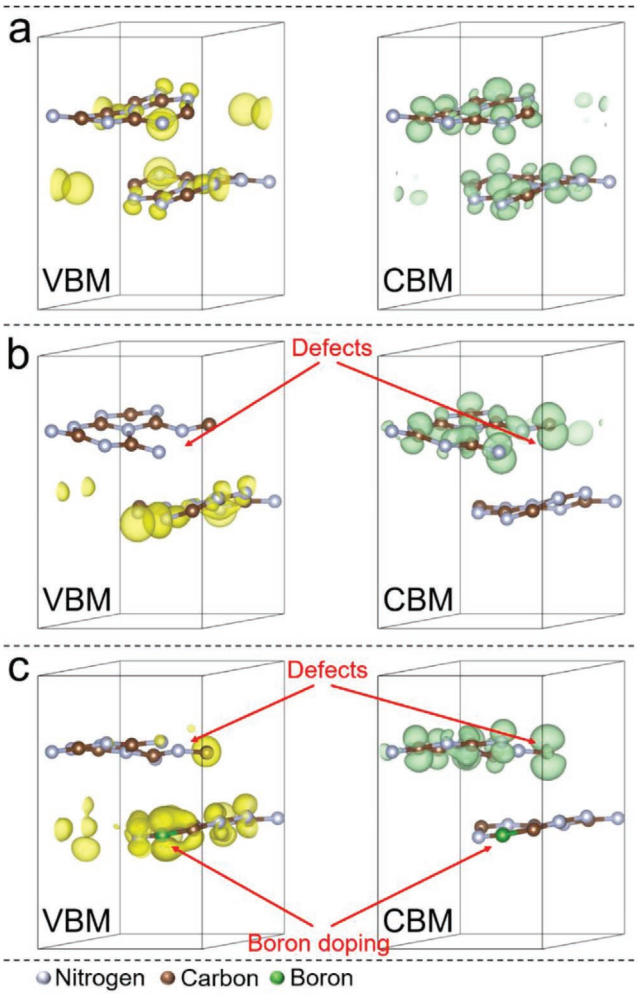

Figure 4. The calculated VBM and CBM of a) pristine g-C_3N_4, b) defected g-C_3N_4, and c) B-doped defected g-C_3N_4.

planar averaged charge density difference were calculated on the two-layer g-C_3N_4 model. As shown in **Figure 6**, the yellow and blue colors denote the electron accumulation and depletion, respectively. The pristine g-C_3N_4 exhibits a highly symmetrical charge distribution on the two layers (Figure 6a), revealing the difficult interlayer electron transfer. And obviously, after the introduction of defect sites, the charge distribution changes significantly (Figure 6b). The 3D charge density difference shows that the electrons tend to accumulate at the defect sites, and the planar average charge difference indicates that the interlayer electron transfer occurs from the non-defected layer to the defected layer. Furthermore, when the B is doped in the down layer, both the defect sites and B-doping sites can attract electrons and form electron accumulation areas. Interestingly, those electron accumulation areas overlap between layers, indicating the photoexcited electrons can transfer across the interlayer through the overlapped areas which can act as an interlayer electronic channel. The corresponding planar average charge density difference shows that the interlayer separation of charge carriers in model is enhanced significantly compared to the above two models. The electrons tend to transfer from the B doped layer to the defected layer, which is highly consistent with the simulated result in Figure 4 that the B doped site has more excitable electrons. The DFT simulated results strongly verify that the synergistic effect between the defect sites and the B doping sites can significantly enhance the interlayer charge transfer of g-C_3N_4, thus greatly promoting charge separation and transfer.

As the photocatalytic performance is determined by the combined action of optical absorption (η_{abs}), charge carrier separation (η_{sep}), and surface charge transfer efficiency (η_{trans}) for a photocatalyst, the η_{trans} is also a very important factor to be evaluated. Herein, with $MVCl_2$ as a fast electron scavenger, the η_{trans} of CN and CNx samples was investigated by elaborately designed photoelectrochemical tests (photocurrent response and LSV tests).[19] As shown in **Figure 7**a, the CN and CN4 samples exhibit photocurrent density at 0.097 and 0.258 μA cm^{-2} in normal electrolyte, respectively. The photocurrent density here can be described by the following equation:

$$J_{H_2O} = J_{max} \times \eta_{abs} \times \eta_{sep} \times \eta_{trans} \quad (2)$$

While in Figure 7b, the current densities rise to 0.369 and 0.536 μA cm^{-2} in the presence of MV^{2+} for CN and CN4 samples. Considering that the surface charge transfer is very fast so that the η_{trans} almost reaches 100%, the current density in this condition can be counted as following equation:

$$J_{MV} = J_{max} \times \eta_{abs} \times \eta_{sep} \quad (3)$$

As the J_{max}, η_{abs}, and η_{sep} are unchanged for the J_{H_2O} and J_{MV}, the η_{trans} can be calculated by the following equation:

$$\eta_{trans} = J_{H_2O}/J_{MV} \quad (4)$$

Here, the η_{trans} of CN and CN4 were calculated to be 26.3% and 48.1%, respectively, indicating that the CN4 sample exhibits much higher surface charge transfer efficiency than pristine CN. That is to say, the CN4 sample possesses faster injection efficiency for photoexcited charge carriers into the reaction system and results in the enhanced photocatalytic performance. In addition, the density of charge carriers of CN and CN4 samples was also determined by the MV^{2+} controlled LSV tests. The charge carriers can transfer to the external circuit once the applied bias voltage reaches the quasi Fermi level since there is hardly any over potential for the reduction of fast electron acceptor MV^{2+}. As shown in Figure 7c, the potential of CN4 (–0.138 V vs Ag/AgCl) is 0.076 V positive than that of CN samples (–0.214 vs Ag/AgCl), so the carrier density difference between CN and CN4 in the quasi Fermi level can be calculated by the following equation:

$$E_{f1} - E_{f2} = kT\ln(N_{f1}/N_{f2})/e \quad (5)$$

where the E_f and N_f are the quasi Fermi level and corresponding carrier density of sample, k is the Boltzmann constant, T is the system temperature during the test and e is elementary charge. The 0.076 V increment is corresponding to 18.9 times higher carrier density in the CN4 samples compared to pristine CN. The work function of pure and modified

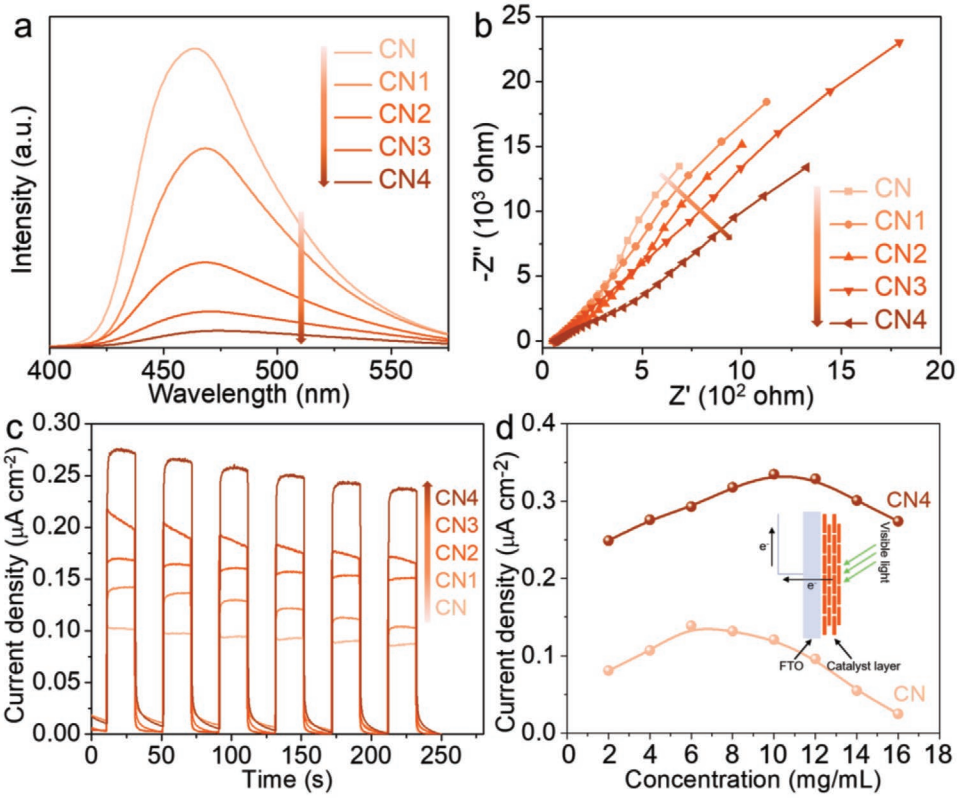

Figure 5. a) Photoluminescence (PL) spectra, b) electrochemical impedance spectroscopy (EIS) Nyquist plots, and c) transient photocurrent response of CN and CN*x*. Concentration dependence of maximun photocurrent density for CN and CN4 on FTO.

g-C_3N_4 was calculated by DFT to evaluate the minimum energy for electrons to escape from the Fermi level into vacuum. As shown in Figure 7d, the Fermi level of pristine g-C_3N_4, defected g-C_3N_4, and B-doped defected g-C_3N_4 were calculated to be −1.26, −0.93, and −1.07 eV, respectively. As the work function is determined by the equation $\Phi = E_V - E_F$, where the E_V and E_F are the potential of vacuum and Fermi level, the work function of pristine g-C_3N_4, defected g-C_3N_4, and B-doped defected g-C_3N_4 were calculated to be 5.51, 5.18, and 5.32 eV, respectively. Although the introduction of B will increase the work function, the work function of B-doped defected g-C_3N_4 is still below that of the pristine one, which facilitates the escaping of the electrons from the g-C_3N_4 surface.

The photocatalytic performances for H_2O_2 evolution of CN and CN*x* were evaluated in an O_2-equilibrated condition under visible light ($\lambda \geq 420$ nm) irradiation. As shown in **Figure 8**a, the pristine CN owns a H_2O_2 evolution rate of 87×10^{-6} M h^{-1}, indicating that the dissolved O_2 was successfully reduced to H_2O_2. The H_2O_2 yield of CN*x* samples were much higher than that of pristine CN and increased from 175 to 287×10^{-6} M h^{-1} with the increase of KBH_4 dosage, and the CN4 samples show the best photocatalytic performance for H_2O_2 yield about 3.3 times higher than that of the pristine CN. Meanwhile, Figure S15b (Supporting Information) shows that the CN4 samples exhibit about 1.5 and 2 times the H_2O_2 yield of DCN and BCN, respectively, proving that the synergistic effect of defects and B doping is indeed more conducive to the improvement of the capacity of g-C_3N_4 to produce H_2O_2. To evaluate the effect of light condition on the evolution of H_2O_2, the apparent quantum yield (AQY) of CN4 was obtained with four wavelengths and shown in Figure 8b. Table S1 (Supporting Information) shows the H_2O_2 yield, light intensity, and calculated AQY with the four monochromatic light irradiations. Obviously, the CN4 sample exhibits excellent AQY in visible range, reaching 27.8% at 420 nm, and the AQY values at 450, 500, and 550 nm are 5.7%, 2.2%, and 1.6%, respectively, which is much higher than many other current photocatalysts with the similar reaction conditions. Since the produced H_2O_2 can react with the CB electron or VB hole, the photocatalysis production of H_2O_2 is a dynamic process of both generation and decomposition. So, the investigation for the decomposition behavior of H_2O_2 over the prepared samples is necessary. The rate constants for H_2O_2 formation (K_f, $\times 10^{-6}$ M min^{-1}) and decomposition (K_d, min^{-1}) over CN and CN*x* samples were first evaluated by assuming zero-order and first-order kinetics, respectively. Values of K_f and K_d are obtained by fitting the H_2O_2 evolution data in Figure 8a to the following equation, and the results are displayed in Figure S16a (Supporting Information).

$$[H_2O_2] = K_f / K_d \times \{1 - \exp(-K_d \times t)\} \tag{6}$$

As shown in Figure S16a (Supporting Information), the K_f value increased from 1.401 to 4.648×10^{-6} M min^{-1}. The 3.32-fold enhancement of K_f indicates the significantly enhanced H_2O_2 formation efficiency of CN4 samples, and the reduced K_d indicates that the modified samples can stabilize the formed

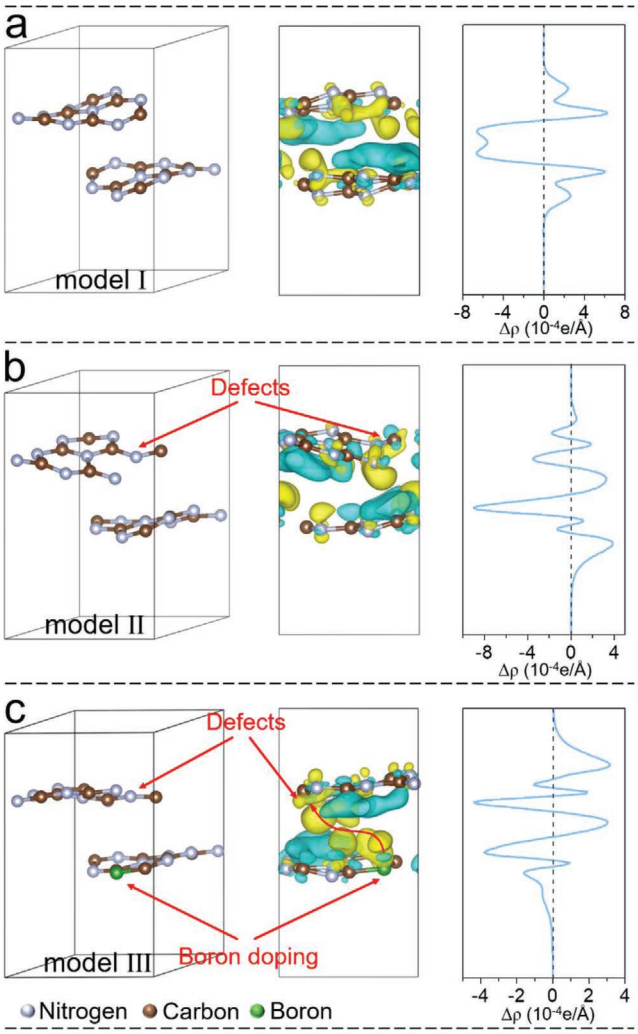

Figure 6. The optimized structure, 3D charge density difference, and planar averaged charge density difference for a) pristine g-C_3N_4, b) defected g-C_3N_4, and c) B-doped defected g-C_3N_4.

H_2O_2 under light irradiation. The H_2O_2 decomposition experiments were also performed and shown in Figure S16b (Supporting Information). The 60 min decomposition of H_2O_2 over CN*x* samples are lower than that over the pristine CN samples, which confirms the above inference. Particularly, the comparison for H_2O_2 production with other current photocatalyst is listed in Table S2 (Supporting Information), and the standardized yield comparison is displayed in Figure 8d. The comparison shows that the CN4 photocatalyst in this work is obviously better than most known catalysts under that same reaction time, catalyst dosage, and light conditions, suggesting that this B-doped defected g-C_3N_4 is a promising photocatalyst for H_2O_2 production. The H_2O_2 evolution without isopropanol was also evaluated in an O_2-equilibrated water under visible light irradiation. As shown in Figure S17 (Supporting Information), the pristine CN sample exhibits almost no capacity to produce H_2O_2 without isopropanol, while the CN*x* samples still have stable H_2O_2 production efficiency, which demonstrated the great potential of the prepared catalysts in photocatalytic H_2O_2 evolution. Considering that the stability of the photocatalyst is a very important property, the cycle experiments for CN4 were performed and shown in Figure 8c. The H_2O_2 yield shows no significant decrease after three consecutive cycles, indicating the outstanding recyclability and physicochemical stability of CN4 photocatalysts.

In order to understand the greatly enhanced photocatalytic performance and the generation mechanism of H_2O_2, the conditional control experiment was carried out first. As shown in Figure S18 (Supporting Information), the H_2O_2 evolution experiment of CN4 was carried out under normal reaction conditions, N_2 bubbling and the addition of $\cdot O_2^-$ scavenger (BQ). The production of H_2O_2 decreased significantly when N_2 was continuously injected, which was about one third of the normal amount, indicating that the dissolved oxygen was the raw material. Since the liquid level is contact with air during the reaction, the dissolved oxygen cannot be completely removed, resulting in production of a certain amount of H_2O_2. However, the H_2O_2 production is negligible in the presence of BQ. In order to exclude the effect of BQ on the iodometry, we prepared two H_2O_2 solutions of the same concentration (300 μmol L^{-1}) and added BQ to one of them. After titration and full coloration, the H_2O_2 concentrations of both solutions were determined to be both 300 μmol L^{-1}, indicating that the presence of BQ would not affect the iodometry. Therefore, it can be concluded that BQ prevents the production of H_2O_2 by consuming the $\cdot O_2^-$, indicating that the $\cdot O_2^-$ is a necessary intermediate for the production of H_2O_2. The ESR spin-trap technology was performed to confirm the existence of $\cdot O_2^-$, as shown in Figure 8e, CN4 exhibits enhanced DMPO-$\cdot O_2^-$ signal than that of pristine CN, indicating the enhanced $\cdot O_2^-$ production capability of CN4. It is well known that O_2 takes an electron to convert to a $\cdot O_2^-$, and the $\cdot O_2^-$ takes another electron to convert to H_2O_2. Hence the average electron number (*n*) involved in the overall O_2 reduction is a key index to measure the evolution efficiency of H_2O_2. Figure 8f and Figure S19 (Supporting Information) illustrate the linear sweep voltammetry curves of CN and CN4 obtained on a rotating disk electrode with different rotate speeds. The Koutecky–Levich plots based on the current density data at –1.0 V versus Ag/AgCl were displayed in the inset of Figure 8f, and the *n* values of CN and CN4 were determined by the slopes of linear regression to be 1.315 and 1.857, respectively. The obtained *n* values indicate that both one-electron oxygen reduction and two-electron oxygen reduction occurred over CN and CN4, while the electron transfer of CN4 is more selective toward two-electron transfer for the H_2O_2 evolution. In addition, considering that the binding of H^+ is a necessary step in the transformation of $\cdot O_2^-$ into H_2O_2, the adsorption capacity of catalyst for H^+ will directly affect the conversion efficiency of H_2O_2. The H^+ adsorption energies of different samples were calculated and shown in Figure S20 (Supporting Information). Obviously, the negative adsorption energies of all the catalysts indicate that they all have adsorption capacities for H^+, while the defect sites and B doping sites exhibit greater H^+ adsorption capacity, which may be attributed to the higher electron density on their surfaces. The stronger H^+ adsorption capacity enables catalyst to accumulate more H^+ on its surface, so that it greatly promotes the transformation of $\cdot O_2^-$ into H_2O_2 and increases the efficiency of two-electron oxygen reduction. Hence, the

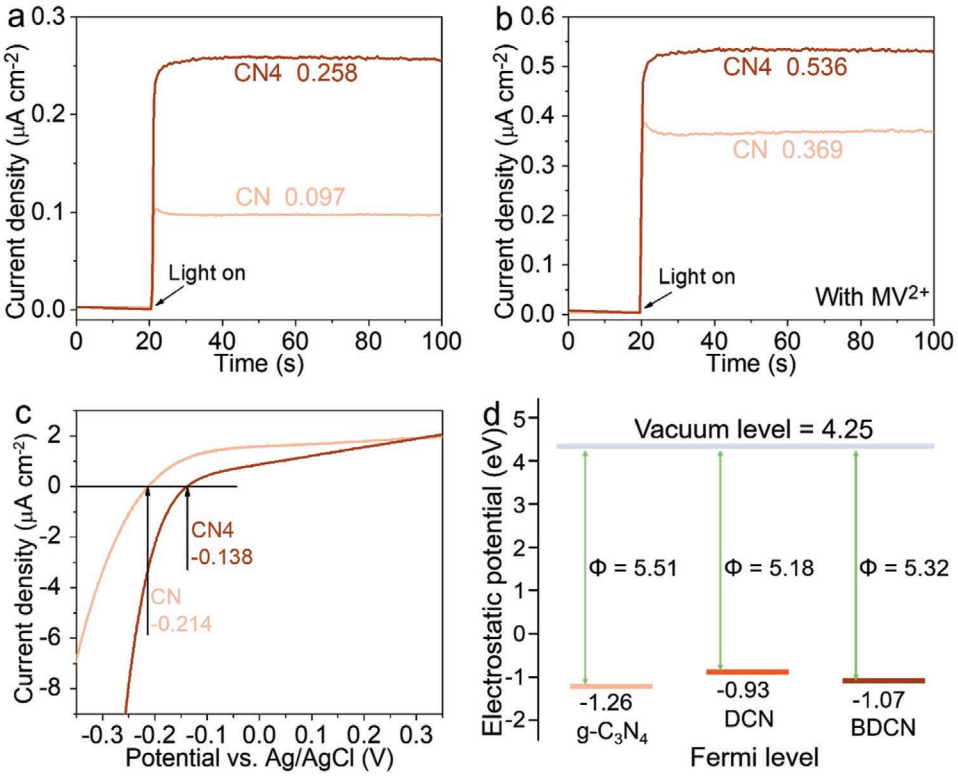

Figure 7. Photocurrent density of CN and CN4 under visible light irradiation a) without and b) with $MVCl_2$. c) Linear sweep voltammetry (LSV) of CN and CN4 under visible light irradiation with $MVCl_2$. d) The calculated work function of pristine g-C_3N_4, defected g-C_3N_4 (DCN) and B-doped defected g-C_3N_4 (BDCN).

H_2O_2 evolution process over CN and CN4 can be proposed and displayed in Figure 8g. For pristine CN, when dissolved oxygen is reduced by electrons to form $\cdot O_2^-$, only a few parts of $\cdot O_2^-$ are further reduced into H_2O_2. However, for the CN4 photocatalysts, not only the $\cdot O_2^-$ production capability is enhanced, but also the conversion rate from $\cdot O_2^-$ to H_2O_2 is also greatly improved, resulting in an efficient and highly selective two-electron (two-step) H_2O_2 evolution.

3. Conclusions

In summary, defect and boron doping sites were successfully introduced into g-C_3N_4 via a KBH_4-assisted thermal polymerization method. The obtained CN*x* samples own leaf-vein-like structures with tunable optical absorption and charge transfer properties, which exhibit excellence performance as a visible-light photocatalyst for the evolution of H_2O_2. The improved photocatalytic performance can be attributed to the large specific surface area, improved optical absorption, enhanced charge transfer and separation, and highly selective two-electron O_2 reduction process. The AQY for H_2O_2 evolution over CN4 is 27.8% at 420 nm, which is much higher than many other current literature values. Throughout this work, the DFT calculation is applied to describe the relationship between the improved photocatalytic performance and the introduced defect and boron doping sites based on the experimental results. This work demonstrates a promising strategy for highly selective two-electron photocatalytic H_2O_2 evolution and provides directions for the preparation of efficient novel photocatalysts.

4. Experimental Section

Preparation of Catalysts: All the chemicals used here are of analytical grade and commercially available. All the aqueous solutions referred are prepared using deionized water.

The pristine graphitic carbon nitride (CN) was prepared as following process. Typically, 10 g melamine was put into a covered ceramic crucible and heated to 520 °C at a rate of 2.5 °C min^{-1} and maintained at 520 °C for 4 h. After cooling to ambient temperature, the yellow agglomerates (CN) were obtained and grounded into powder.

The leaf-vein-like g-C_3N_4 photocatalysts were synthesized as follows: 10 g of melamine and a certain amount of KBH_4 were ground and mixed fully. Then the mixture was transferred into a horizontal tube furnace and heated to 520 °C with a heating rate of 5 °C min^{-1} under nitrogen atmosphere, and kept at this temperature for 4 h. Products were denoted as CN*x* (where x = 1, 2, 3, and 4 corresponds to the KBH_4 dosage of 0.1, 0.5, 1, and 2 g). All samples were washed with water and alcohol for three times.

The defected g-C_3N_4 or B doped g-C_3N_4 samples were synthesized with the same process except replacing the KBH_4 with KOH or B_2O_3, respectively.

Characterization: The phase structures of as-prepared samples were studied by X-ray diffractometry (XRD) measurement on a Bruker AXS D8 advance X-ray diffractometer with Cu-Kα irradiation (40 kV/40 mA). The atomic contents of samples were determined by organic element analyzer (OEA, Elementar vario MACRO cube) and inductively coupled plasma optical emission spectrometer (ICP-OES, Agilent 725). The morphologies and microstructures were investigated by

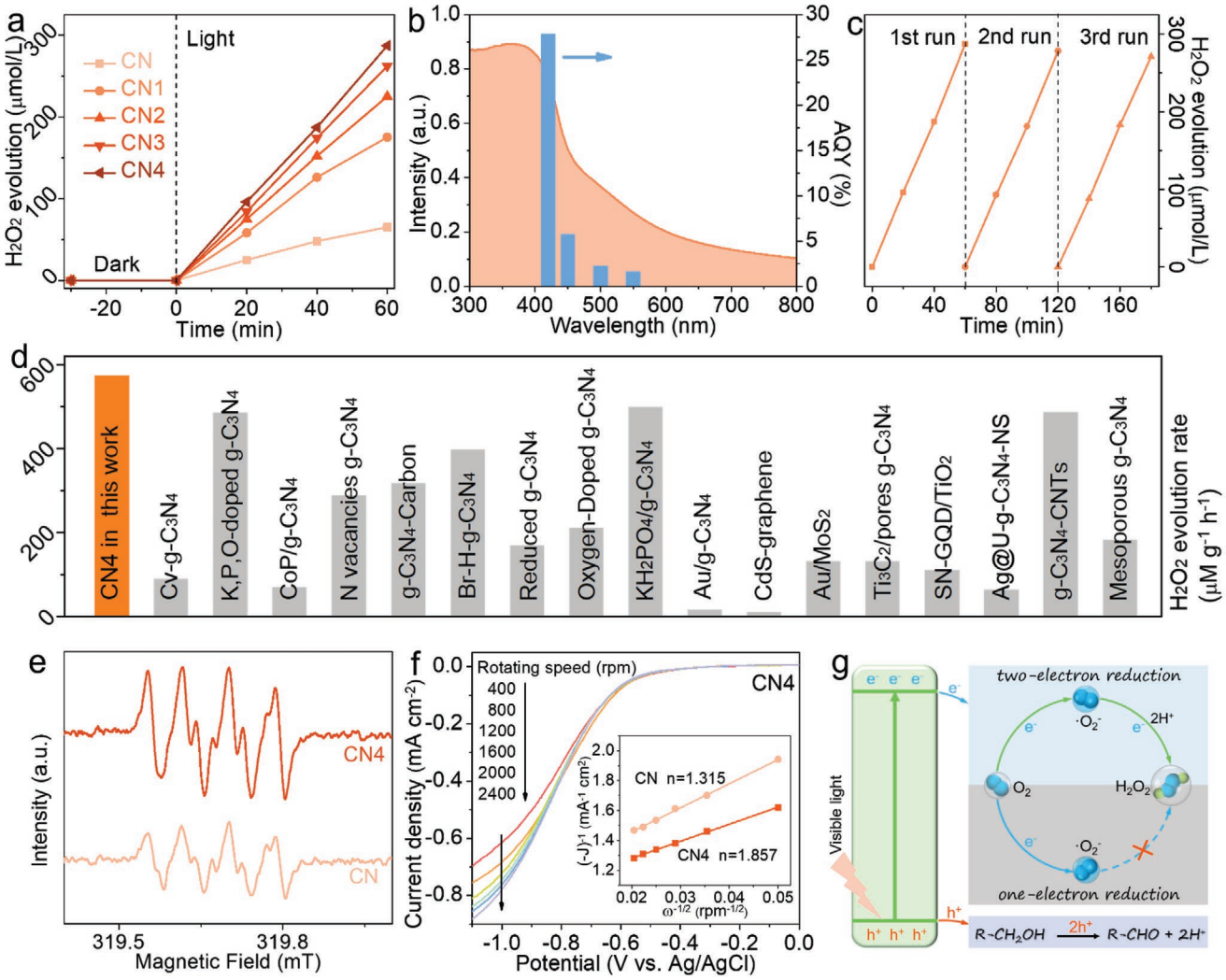

Figure 8. a) Time course of H_2O_2 production for prepared photocatalysts under visible light irradiation. b) DRS (left axis) of CN4 and apparent quantum yield (AQY, right axis) of photocatalytic H_2O_2 production with monochromatic light irradiation. c) Cycling runs for the photocatalytic H_2O_2 production over CN4. d) Comparison for H_2O_2 production with other photocatalysts in recent works. e) ESR signals of DMPO-·O_2^- over CN and CN4 under visible light. f) LSV curves of CN4 measured on RDE at different rotating speeds. Inset: the corresponding Koutecky–Levich plots of CN and CN4. g) Proposed mechanism for enhanced H_2O_2 production.

Gemini 300 scanning electron microscopy (SEM, Zeiss), F20 S-TWIN transmission electron microscopy (TEM, Tecnai G2, FEI Co), and Bruker Dimension Edge atomic force microscopy (AFM). The surface chemical compositions were analyzed by X-ray photoelectron spectroscopy (XPS, ESCALAB 250Xi, Thermo Fisher). The specific surface areas of samples were determined via a N_2 adsorption–desorption and Brunauer–Emmett–Teller (BET) method by a surface area analyzer (NOVA 2200e, Quantachrome). The diffuse reflectance absorption spectra (DRS) of samples were measured by a UV–vis spectrophotometer (Cary 300, USA) with an integrating sphere attachment and $BaSO_4$ reference. The photoluminescence (PL) spectroscopy was measured by a Hitachi-7000 fluorescence spectrometer with an excitation wavelength of 350 nm at room temperature.

Photoelectrochemical Measurements: The electrochemical and photoelectrochemical measurements were recorded by a CHI 660D workstation in a three-electrode cell. A Pt electrode and an Ag/AgCl electrode were used as the counter and reference electrode, respectively. An FTO (active area of 1 cm^2) electrode covered with samples was used as the working electrode. A 300 W Xe lamp was used as light source. The transient photocurrent response, electrochemical impedance spectroscopy (EIS), and linear sweep voltammetry (LSV) curves of samples were measured with 0.1 M Na_2SO_4 electrolyte solution. Methylviologen dichloride ($MVCl_2$, 1×10^{-3} M) was added into the electrolyte as a fast electron scavenger to investigate the surface charge transfer efficiency. The working electrode was prepared through a simple drop-casting method. Typically, 4.0 mg of prepared photocatalyst was dispersed in 1.0 mL of ethanol (with 0.05% Nafion) and ultrasonicated for 1 h. Then, 200 μL of the above suspension was dripped onto FTO electrode (1 × 2 cm) and dried to form a film.

The rotating disk electrode (RDE) measurements were performed on a Model 636A electrochemical system by Princeton Parstat3000A-DX workstation with an Ag/AgCl electrode and a Pt electrode as reference and counter electrode, respectively. The LSV curves were obtained in an O_2-saturated 0.1 M phosphate buffer solution (pH = 7). During the whole test process, O_2 was kept flowing on the liquid surface of the electrolyte. The average transfer electron number (n) in the overall O_2 reduction was obtained by the slopes of Koutecky–Levich plots with the following equation:

$$j^{-1} = j_k^{-1} + B^{-1}\Omega^{-1/2} \quad (7)$$

$$B = 0.2nFv^{-1/6}CD^{2/3} \quad (8)$$

where j, j_k, and Ω are the tested current density, kinetic current density, and rotating speed (rpm), respectively. F and ν are the Faraday constant (96 485 C mol^{-1}) and kinetic viscosity of water (0.01 cm^2 s^{-1}), C and D are the bulk concentration of O_2 in water (1.26×10^{-3} mol cm^{-3}) and the diffusion coefficient of O_2 (2.7×10^{-5} cm^2 s^{-1}).

Theoretical Calculations: The first-principle calculations were performed within the framework of density-functional-theory (DFT) as implemented in the Vienna Ab-initio Simulation Package (VASP). The exchange–correlation interactions were treated by generalized gradient approximation (GGA) parameterized by Perdew, Burke, and Ernzerhof (PBE). The interaction between ions and electrons was described using the projected augmented wave (PAW) formalism with an energy cutoff of 400 eV. All the structures were fully relaxed until the force on each atom was less than 0.01 eV Å^{-1}. The H^+ adsorption energies (ΔE_{ads} eV) were calculated by the following equation:

$$\Delta E_{ads} = E(^*H^+) - E(^*) - 1/2E(H_2) \quad (9)$$

where ΔE_{ads} is the adsorption energy, E is the optimized energy from DFT, and * is defined as adsorption site.

Photocatalytic Reduction of Oxygen to H_2O_2: Typically, 50 mg of as-synthesized photocatalyst was dispersed in 100 mL isopropanol aqueous solution (10%). The suspension solutions were stirred for 30 min in the dark with continually O_2 bubbling after ultrasound treatment for 10 min to reach the absorption–desorption equilibrium. Then the solutions were exposed to visible light provided by a 300 W Xe lamp with a 420 nm cutoff filter. The light source was located at a distance of 10 cm from the reactor, and a continuous magnetic stirrer and cooling water were applied during the experiment. During illumination, 3 mL solution was sampled every 10 min and filtrated with a 0.45 µm to remove the photocatalyst. To investigate the decomposition behavior of H_2O_2 over prepared photocatalysts, 50 mg of as-synthesized photocatalyst was dispersed in 100 mL 1×10^{-3} M H_2O_2 solution and irradiated under visible light for 60 min with continuous stirring.

The amount of H_2O_2 was analyzed by iodometry.[20] Typically, 1 mL of 0.1 mol L^{-1} $C_8H_5KO_4$ aqueous solution and 1 mL of 0.4 mol L^{-1} potassium iodide (KI) aqueous solution were added to obtained solution, and kept for 30 min. The H_2O_2 molecules reacted with iodide anions (I^-) under acidic conditions ($H_2O_2 + 3I^- + 2H^+ \rightarrow I_3^- + 2H_2O$) to produce triiodide anions (I_3^-) possessing a strong absorption at around 350 nm. The amount of I_3^- was determined by means of UV–vis spectroscopy on the basis of the absorbance at 350 nm, from which the amount of H_2O_2 produced during each reaction was estimated.

Supporting Information

Supporting Information is available from the Wiley Online Library or from the author.

Acknowledgements

The study was financially supported by Projects 51579096, 51521006, and 51909089 supported by National Natural Science Foundation of China, the Funds for Innovative Province Construction of Hunan Province (2019RS3012), the Key Research and Development Program of Hunan Province of China (2017SK2241), the National Innovative Talent Promotion Program of China (2017RA2088).

Conflict of Interest

The authors declare no conflict of interest.

Keywords

boron doping, defects, g-C_3N_4, H_2O_2 evolution, two-electron oxygen reduction

Received: February 29, 2020
Revised: May 30, 2020
Published online:

[1] J. K. Edwards, B. Solsona, E. Ntainjua, A. F. Carley, A. A. Herzing, C. J. Kiely, G. J. Hutchings, *Science* **2009**, *323*, 1037.

[2] a) Y. Kofuji, Y. Isobe, Y. Shiraishi, H. Sakamoto, S. Tanaka, S. Ichikawa, T. Hirai, *J. Am. Chem. Soc.* **2016**, *138*, 10019; b) S. Fukuzumi, Y. Yamada, K. D. Karlin, *Electrochim. Acta* **2012**, *82*, 493; c) K. Mase, M. Yoneda, Y. Yamada, S. Fukuzumi, *Nat. Commun.* **2016**, *7*, 11470; d) A. Gervasini, P. Carniti, F. Desmedt, P. Miquel, *ACS Catal.* **2017**, *7*, 4741.

[3] a) J. M. Campos-Martin, G. Blanco-Brieva, J. L. Fierro, *Angew. Chem., Int. Ed.* **2006**, *45*, 6962; b) Z. Zheng, Y. H. Ng, D. W. Wang, R. Amal, *Adv. Mater.* **2016**, *28*, 9949; c) N. M. Wilson, D. W. Flaherty, *J. Am. Chem. Soc.* **2016**, *138*, 574.

[4] a) D. Tsukamoto, A. Shiro, Y. Shiraishi, Y. Sugano, S. Ichikawa, S. Tanaka, T. Hirai, *ACS Catal.* **2012**, *2*, 599; b) L. Zheng, H. Su, J. Zhang, L. S. Walekar, H. V. Molamahmood, B. Zhou, M. Long, Y. H. Hu, *Appl. Catal., B* **2018**, *239*, 475; c) M. Teranishi, R. Hoshino, S. I. Naya, H. Tada, *Angew. Chem., Int. Ed.* **2016**, *55*, 12773; d) Y. Shiraishi, S. Kanazawa, Y. Sugano, D. Tsukamoto, H. Sakamoto, S. Ichikawa, T. Hirai, *ACS Catal.* **2014**, *4*, 774.

[5] a) H. Hou, X. Zeng, X. Zhang, *Angew. Chem., Int. Ed.* **2020**, *59*, 2; b) X. Zeng, Y. Liu, Y. Kang, Q. Li, Y. Xia, Y. Zhu, H. Hou, M. H. Uddin, T. R. Gengenbach, D. Xia, C. Sun, D. T. Mccarthy, A. Deletic, J. Yu, X. Zhang, *ACS Catal.* **2020**, *10*, 3697; c) W. Hou, Y. Li, S. Ouyang, H. Chen, J. Ye, X. Han, Y. Deng, *Chem. Commun.* **2019**, *55*, 13279.

[6] a) J. Liu, Y. Liu, N. Liu, Y. Han, X. Zhang, H. Huang, Y. Lifshitz, S.-T. Lee, J. Zhong, Z. Kang, *Science* **2015**, *347*, 970; b) X. Wang, X. Chen, A. Thomas, X. Fu, M. Antonietti, *Adv. Mater.* **2009**, *21*, 1609; c) Y. Zhao, X. Min, Z. Ding, S. Chen, C. Ai, Z. Liu, T. Yang, X. Wu, Y. Liu, S. Lin, Z. Huang, P. Gao, H. Wu, M. Fang, *Adv. Sci.* **2020**, *7*, 1902051.

[7] a) G. Gao, Y. Jiao, E. R. Waclawik, A. Du, *J. Am. Chem. Soc.* **2016**, *138*, 6292; b) R. Kuriki, K. Sekizawa, O. Ishitani, K. Maeda, *Angew. Chem., Int. Ed.* **2015**, *54*, 2406.

[8] a) C. Ling, X. Niu, Q. Li, A. Du, J. Wang, *J. Am. Chem. Soc.* **2018**, *140*, 14161; b) Q. Liu, L. Ai, J. Jiang, *J. Mater. Chem. A* **2018**, *6*, 4102.

[9] a) C. Feng, Y. Deng, L. Tang, G. Zeng, J. Wang, J. Yu, Y. Liu, B. Peng, H. Feng, J. Wang, *Appl. Catal., B* **2018**, *239*, 525; b) L. Tang, C. Feng, Y. Deng, G. Zeng, J. Wang, Y. Liu, H. Feng, J. Wang, *Appl. Catal., B* **2018**, *230*, 102.

[10] a) Z. Wei, M. Liu, Z. Zhang, W. Yao, H. Tan, Y. Zhu, *Energy Environ. Sci.* **2018**, *11*, 2581; b) Y. Shiraishi, Y. Kofuji, H. Sakamoto, S. Tanaka, S. Ichikawa, T. Hirai, *ACS Catal.* **2015**, *5*, 3058; c) Y. Kofuji, S. Ohkita, Y. Shiraishi, H. Sakamoto, S. Tanaka, S. Ichikawa, T. Hirai, *ACS Catal.* **2016**, *6*, 7021; d) J. Cai, J. Huang, S. Wang, J. Iocozzia, Z. Sun, J. Sun, Y. Yang, Y. Lai, Z. Lin, *Adv. Mater.* **2019**, *31*, 1806314; e) S. Zhao, X. Zhao, H. Zhang, J. Li, Y. Zhu, *Nano Energy* **2017**, *35*, 405.

[11] a) D. Zheng, X. N. Cao, X. Wang, *Angew. Chem., Int. Ed.* **2016**, *55*, 11512; b) Y. Zeng, X. Liu, C. Liu, L. Wang, Y. Xia, S. Zhang, S. Luo, Y. Pei, *Appl. Catal., B* **2018**, *224*, 1.

[12] a) J. Zhang, J. Sun, K. Maeda, K. Domen, P. Liu, M. Antonietti, X. Fu, X. Wang, *Energy Environ. Sci.* **2011**, *4*, 675; b) M. Bellardita,

E. I. García-López, G. Marcì, I. Krivtsov, J. R. García, L. Palmisano, *Appl. Catal., B* **2018**, *220*, 222.

[13] a) M. Zhu, S. Kim, L. Mao, M. Fujitsuka, J. Zhang, X. Wang, T. Majima, *J. Am. Chem. Soc.* **2017**, *139*, 13234; b) C. Marchal, T. Cottineau, M. G. Méndez-Medrano, C. Colbeau-Justin, V. Caps, V. Keller, *Adv. Energy Mater.* **2018**, *8*, 1702142; c) Z. Zhang, J. Huang, Y. Fang, M. Zhang, K. Liu, B. Dong, *Adv. Mater.* **2017**, *29*, 1606688.

[14] a) H. Yu, R. Shi, Y. Zhao, T. Bian, Y. Zhao, C. Zhou, G. I. Waterhouse, L. Z. Wu, C. H. Tung, T. Zhang, *Adv. Mater.* **2017**, *29*, 1605148; b) W. Wang, H. Zhang, S. Zhang, Y. Liu, G. Wang, C. Sun, H. Zhao, *Angew. Chem., Int. Ed.* **2019**, *58*, 16644.

[15] a) Y. Zhao, L. Yang, S. Cheng, X. Wang, Y. Ma, Q. Wu, Y. Jiang, W. Qian, Z. Hu, *J. Am. Chem. Soc.* **2013**, *135*, 1201. b) K. Chandran, P. C. Clinsha, M. Lavanya, S. Anthonysamy, K. I. Gnanasekar, *J. Am. Ceram. Soc.* **2019**, *102*, 2932; c) T. Shirasaki, A. Derré, M. Ménétrier, A. Tressaud, S. Flandrois, *Carbon* **2000**, *38*, 1461.

[16] a) Y. Xie, Y. Li, Z. Huang, J. Zhang, X. Jia, X. Wang, J. Ye, *Appl. Catal., B* **2020**, *265*, 118581; b) Y. Fu, C. Liu, M. Zhang, C. Zhu, H. Li, H. Wang, Y. Song, H. Huang, Y. Liu, Z. Kang, *Adv. Energy Mater.* **2018**, *8*, 1802525; c) L. Tang, X. Ouyang, B. Peng, G. Zeng, Y. Zhu, J. Yu, C. Feng, S. Fang, X. Zhu, J. Tan, *Nanoscale* **2019**, *11*, 12198.

[17] a) C. Chu, Q. Zhu, Z. Pan, S. Gupta, D. Huang, Y. Du, S. Weon, Y. Wu, C. Muhich, E. Stavitski, K. Domen, J. Kim, *Proc. Natl. Acad. Sci. U. S. A.* **2020**, *117*, 6376; b) C. Feng, L. Tang, Y. Deng, J. Wang, Y. Liu, X. Ouyang, Z. Chen, H. Yang, J. Yu, J. Wang, *Appl. Catal., B* **2020**, *276*, 119167.

[18] G. Zhang, G. Li, Z. A. Lan, L. Lin, A. Savateev, T. Heil, S. Zafeiratos, X. Wang, M. Antonietti, *Angew. Chem., Int. Ed.* **2017**, *56*, 13445.

[19] a) J. C. Hill, A. T. Landers, J. A. Switzer, *Nat. Mater.* **2015**, *14*, 1150; b) C. Feng, L. Tang, Y. Deng, J. Wang, W. Tang, Y. Liu, Z. Chen, J. Yu, J. Wang, Q. Liang, *Chem. Eng. J.* **2020**, *389*, 124474; c) G. Liu, J. Shi, F. Zhang, Z. Chen, J. Han, C. Ding, S. Chen, Z. Wang, H. Han, C. Li, *Angew. Chem., Int. Ed.* **2014**, *53*, 7295; d) C. Liu, H. Huang, L. Ye, S. Yu, N. Tian, X. Du, T. Zhang, Y. Zhang, *Nano Energy* **2017**, *41*, 738; e) C. Feng, L. Tang, Y. Deng, G. Zeng, J. Wang, Y. Liu, Z. Chen, J. Yu, J. Wang, *Appl. Catal., B* **2019**, *256*, 117827.

[20] C. Kormann, D. W. Bahnemann, M. R. Hoffmann, *Environ. Sci. Technol.* **1988**, *22*, 798.